RSC Advances

PAPER

View Article Online
View Journal | View Issue

Cite this: *RSC Adv.*, 2020, **10**, 27688

Deformation mechanism in $Al_{0.1}CoCrFeNi$ Σ3(111) [1$\bar{1}$0] high entropy alloys – molecular dynamics simulations

Cuixia Liu, *[a] Yuchia Yang[b] and Zhenhai Xia[b]

High entropy alloys (HEAs), composed of multiple components with equal or near atomic proportions, have extraordinary mechanical properties and are expected to bear the impact of high-speed forces in armor protection structure materials. In order to understand the deformation behaviour of HEAs under tensile and compressive loading, molecular dynamics simulations were performed to reveal the deformation mechanism and mechanical properties of three crystal structures: $Al_{0.1}CoCrFeNi$ HEAs without grain boundaries (perfect HEAs), $Al_{0.1}CoCrFeNi$ HEAs with grain boundaries of Σ3(111)[1$\bar{1}$0] (GBs HEAs) and grain boundaries of Σ3(111)[1$\bar{1}$0] with chemical cluster HEAs (cluster-GBs HEAs). The mechanical properties of the three models at the same strain rate were discussed. Then, the mechanical properties at different strain rates were analyzed. The movement and direction of internal dislocations during the deformation process were investigated. The simulation results show that the GBs HEAs and the cluster-GBs both play an important role in the deformation and failure of the HEAs. Under tensile loading, three behaviour stages of deformation were observed. Cluster-GBs HEAs have a larger yield strength and Young's modulus than that of GBs and perfect HEAs. The higher the strain rate is, the greater the stress reduction rate. Under compressive loading, there are only two behaviour stages of deformation. Cluster-GBs HEAs also have the largest yield strength. Under tensile and compressive deformation, Shockley partial dislocations of 1/6 <112> are dominant and their moving direction and effect on mechanical properties are discussed.

Received 28th February 2020
Accepted 3rd July 2020

DOI: 10.1039/d0ra01885f

rsc.li/rsc-advances

Introduction

High entropy alloys (HEAs) have attracted much attention owing to their extraordinary engineering properties, such as high strength at elevated temperatures, high hardness, superior ductility, excellent corrosion resistance, good wear resistance and high fatigue resistance.[1–5] High entropy alloys with such excellent performance are expected to replace high-strength armor steel, which can bear the impact of high-speed forces in the armor protection structure of ships.[6] These properties were achieved through multi-component design with equal or nearly atomic proportions to form simple solid-solution microstructures, such as face-centered cubic (FCC), body-centered cubic (BCC) or hexagonal closed-packed (HCP) microstructures. Compared with traditional alloys based on one or two key elements, HEAs contain five or more composition elements, which tend to form larger mixing entropies and become very stable.[7–9] Among all the strengthening mechanisms, grain boundaries as a fundamental surface defect type have significant effects on the mechanical properties of HEAs.[10] The grain size and strain rate of CoCrFeMnNi alloys are the main two factors affecting tensile properties.[11] Sangid *et al.* calculated the energy barriers between slip–GB interactions with a new methodology and drew the stacking fault energy curve for slip in a perfect FCC material.[12] In spite of these explorations of related theories, it is necessary to understand the different roles played by grain boundary in strengthening HEAs compared with traditional alloys.

How the grain boundary affects the deformation behaviour and thus improves the mechanical properties of HEAs becomes a primary question for researchers. In previous work, Yu *et al.* observed that a CrFeCoNiPd alloy had higher continuous steady strain hardening than that in other single-phase HEAs with similar grain sizes at ambient temperature.[13] They also hypothesized that plastic deformation at room temperature was primarily involved in the 1/2 <110> {111} full dislocation. Lu *et al.* simulated the deposition and annealing process of AlCoCrCuFeNi HEAs and observed that a phase of the cluster structure was transformed from BCC to FCC.[14] The clustering in HEAs has a significant effect on the phase transition. Huang *et al.* simulated the glass transition temperature of Al–Cu–Cr–Fe–Ni HEAs using molecular dynamics (MD).[15] Li *et al.*

[a]*School of Materials Science and Chemical Engineering, Xi'an Technological University, Xi'an, Shaanxi 710021, China. E-mail: cuixialiu2016@sina.com*
[b]*Department of Materials Science and Engineering, Department of Chemistry, University of North Texas, Denton, TX 76203, USA*

simulated the structural transformation process of a AlCrCoCuFeNi HEA at different cooling rates by molecular dynamics.[16]

Few studies have focused on the influence of the grain boundary on the strength of high entropy alloys. In order to elucidate the strengthening and toughening mechanisms in HEAs at the micro scale and enhance the mechanical properties for HEAs, the stacking fault for different local atomic configurations in a $Al_xCoCrFeNi$ HEA was calculated.[17] It was interesting that not only negative stacking fault energy (SFE) and negative twin formation energy (TFE), but also notable fluctuations in the SFE and TFE in local regions were found. Dislocation also played an important role in the strengthening of HEAs. Based on this work, classical MD methods were employed to explore the deformation strengthening mechanism of $Al_xCoCrFeNi$ HEAs and the role of grain boundaries (GBs) in the HEAs. The GBs were determined by the coincident site lattice (CSL) method. The CSL of $\Sigma3(111)[1\bar{1}0]$ was observed in HEAs within some experimental research works.[18] The chemical clustering in HEAs has a significant effect on the GB energy and mechanical properties of the HEAs. In order to study the effects of different GBs on the mechanical properties of $Al_{0.1}CoCrFeNi$ HEAs, three models of $Al_{0.1}CoCrFeNi$ HEAs were established and MD simulations were carried out. The first one was the perfect crystal structure of $Al_{0.1}CoCrFeNi$ HEAs, which does not include any GBs (Abbrev. perfect HEAs). The second one was $Al_{0.1}CoCrFeNi$ HEAs with GBs of $\Sigma3(111)[1\bar{1}0]$ (Abbrev. GBs HEAs). The third one has GBs with chemical clusters, which were obtained through performing a simulated annealing MD simulation on $Al_{0.1}CoCrFeNi$ HEAs with GBs of $\Sigma3(111)[1\bar{1}0]$ (Abbrev. cluster-GBs HEAs). The quasi-static stretch of tensile and compressive loading was forced on the above three models to investigate deformation behavior.

Computational details

The first model, perfect HEAs of $Al_{0.1}CoCrFeNi$, was built and relaxed at 25 °C, which kept one grain orientation (shown in Fig. 1). The atoms are colored according to the common neighbor analysis (CNA). In the following figures, the meaning of colors is the same as that of Fig. 1.

The second model was very significant. The interfacial structures of GBs HEAs were established based on the theory of CSL, in which two lattices are intertwined, translated and rotated with each other.[19] When they reach a certain position, such as a special angle, parts of the above two lattices coincide with each other. The coincidence sites form the super lattice of a three-dimensional spatial lattice in space. For example, $\Sigma3(111)[1\bar{1}0]$ indicates that in the mismatch direction in CSL, two grains have 1/3 lattice points coinciding with each other, where (111) is the GB plane and $[1\bar{1}0]$ is the rotating axis contained within the GB plane, as shown in Fig. 2.

In Fig. 2, for the upper grain, the *X*-axis, *Z*-axis and *Y*-axis were $[11\bar{2}]$, $[1\bar{1}0]$, and [111], respectively, while they are [112], $[1\bar{1}0]$, and $[\bar{1}\bar{1}1]$ for the lower grain. The angle between two grains along the *Y*-axis was 109.47°. In the three directions, periodic boundary conditions were enforced. Each GB structure included two-twist grains interacting with each other. To avoid the self-interaction, the size of the GB model should be large enough to neglect the interactions of the boundary's strain field. Energy minimization was carried out to obtain the lowest-energy converged structure for determining the distance between the two twist GBs.[20–23] The 3D structure of the symmetric twist grain boundary for $Al_{0.1}CoCrFeNi$ $\Sigma3(111)[1\bar{1}0]$ HEAs is shown in Fig. 3.

The size of the GB model was calculated based on the following formulas (1) and (2). *L*, *B* and *W* were along the *Y*-axis, *X*-axis and *Z*-axis, respectively in Fig. 3. The minimum distance in the *Y* direction was equal or greater than 8 nm, while the *X* and *Z* direction for every grain was equal or greater than 5 nm.

$$L = a \times \sqrt{h^2 + k^2 + l^2} \geq 8 \text{ nm} \quad (1)$$

$$B \text{ or } W = b \times \sqrt{h^2 + k^2 + l^2} \geq 5 \text{ nm} \quad (2)$$

Where *h*, *k* and *l* are Miller indices for every grain orientation along the three orthogonal vectors, respectively. *a* and *b* are constant to reach the required size.

The generated CSL GBs HEAs, containing about 46 480 atoms, were subjected to energy minimization to obtain their global energy minimum structure. Afterwards, all atoms are in the most stable state of energy. As a consequence, the total GBs were in the minimum energy condition.

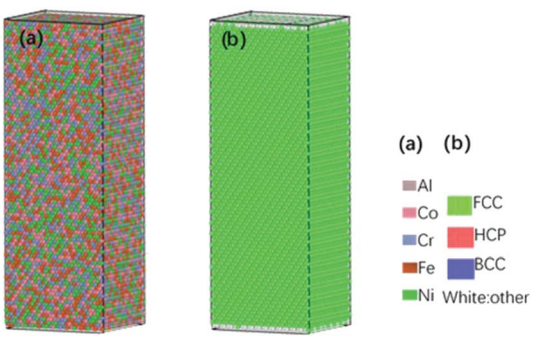

Fig. 1 3D structures of perfect HEAs. (a) Different color means different element. (b) Different color means different crystal structure.

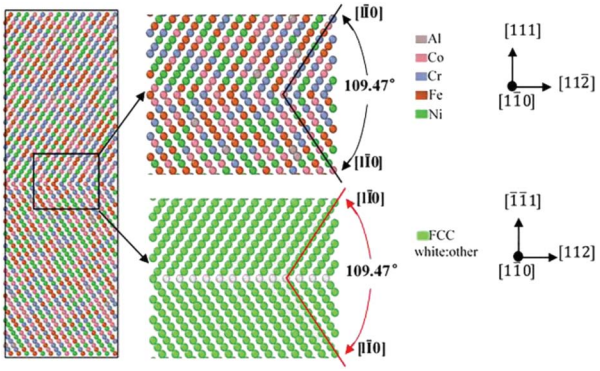

Fig. 2 Structure of CSL symmetric twist GBs for $Al_{0.1}CoCrFeNi$ $\Sigma3(111)$ $[1\bar{1}0]$ HEAs.

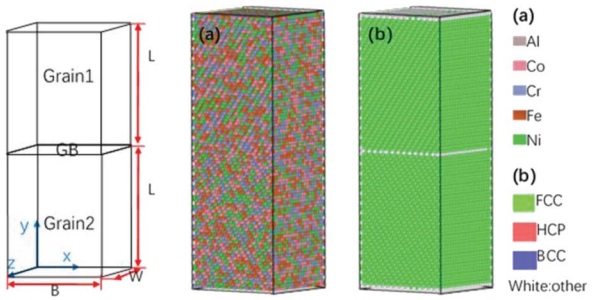

Fig. 3 3D structures of $Al_{0.1}CoCrFeNi$ Σ3(111)[1$\bar{1}$0] symmetric twist grain boundary and GBs HEAs.

The third model was the solid solution including grain boundary under solidification of the second model, the aim of which was to obtain the original GBs of the solid solution with clusters and to study the effect of clustering. During the melting process, the second model was divided into an internal region and an external region (about 10 Å). The external region acted as a seed crystal, causing the internal region to grow into Σ3(111)[1$\bar{1}$0] GBs in the solidification process. Therefore, the internal region should be melted. Since the external region was fixed during melting, the pressure increased, which led to the increase of melting temperature. The melting temperature of this model was 3800 K, which was much higher than the experimental melting point for $Al_{0.1}CoCrFeNi$ HEAs at about 1450 °C.[7] After the model was melted at 3800 K, the internal atoms were relaxed for a long enough time until no clusters were present and they became short-range disordered structures. The variation of diffusion coefficient and morphology with temperature are shown in Fig. 4(a). During the relaxation process, the relationship between the diffusion coefficient and relaxation time is shown in Fig. 4(b).

It can be seen in Fig. 4(a), between 300 K and 3300 K, that the model transforms from the FCC structure to a mixture of BCC and HCP structures. The diffusion coefficient of the model is small ($D = 2.65 \times 10^{-8}$ m^2 s^{-1}) and nearly unchanged. After 3300 K, BCC and HCP structures become more dominant and the diffusion coefficient begins to increase sharply up to 20.8×10^{-8} m^2 s^{-1} at 3800 K. This indicates that the model begins to melt at 3300 K and the atoms change from a long-range ordered structure to short-range disordered structure. In order to save calculation time, the model continues to heat up to 3800 K.

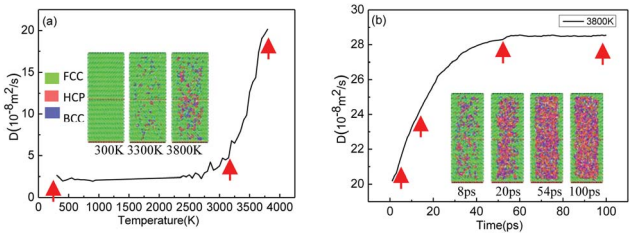

Fig. 4 The variation of diffusion coefficient and morphology with temperature and time for cluster-GBs HEAs. (a) Different temperature. (b) Different time.

In Fig. 4(b), the diffusion coefficient continues to increase as the relaxing time increases until 54 ps where it tends to stabilize to 28.448×10^{-8} m^2 s^{-1}. The morphology also shows that the whole structure is mixed evenly between FCC, BCC and HCP, which indicates that the system is completely melted into a short-range disordered state at this time. With the increase of the relaxation time, the diffusion coefficient maintains a constant value, which indicates that the system is completely melted, and the third model is obtained by cooling the system.

After sufficient quenching time, the model was cooled to room temperature, and then the quenching of atoms formed a crystal structure with GBs, as shown in Fig. 5.

During the process of MD simulations, periodic boundary conditions were applied in the three directions for the above three models. The interatomic interactions were described by an embedded atom method (EAM) proposed by Daw and Baskes.[24,25] Ensemble is another critical factor in the simulation of HEA systems. In the tensile strength process, an isothermal-isobaric ensemble (NPT) was applied at 300 K, while a canonical ensemble (NVT) was enforced in the annealing process to obtain GBs. In a certain temperature range, the equations of motion were integrated with a time step of 0.01 fs using a Large-scale Atomic/Molecular Massively Parallel Simulator (LAMMPS).[26] The visualization software for atomic structure was employed using an Open Visualization Tool (OVITO). The Burgers vector for dislocations in the processing of deformation was determined with the dislocation extraction algorithm (DXA) developed by Stukowski in OVITO.[27]

Results and discussions

The plastic properties are discussed in depth in this section. Based on the above three models, the quasi-static stretch including tensile loading and compressive loading was applied perpendicular to the GB direction with different strain rates including 6.2×10^{10} s^{-1}, 1.2×10^{10} s^{-1}, 6.2×10^{9} s^{-1}, 1.2×10^{9} s^{-1} and 6.2×10^{8} s^{-1}. The mechanical properties of three models at the same strain rate are discussed. Then, the mechanical properties at different strain rates were analyzed. The movement and direction of internal dislocations during the deformation process were investigated.

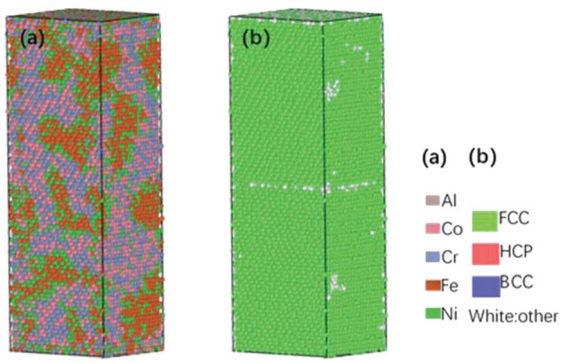

Fig. 5 3D structures of cluster-GBs HEAs.

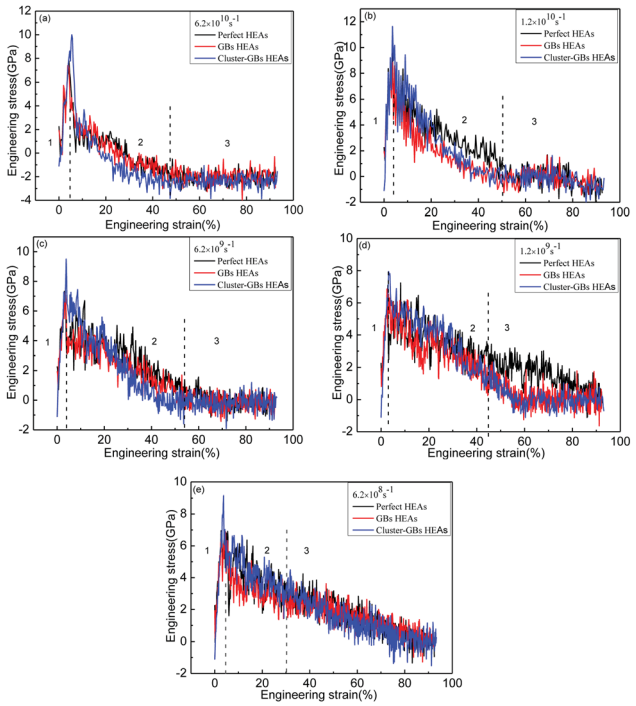

Fig. 6 Tensile engineering stress–strain curves of deformation process oriented in <111> axis under tensile loading at different strain rate for perfect HEAs, GBs HEAs and cluster-GBs HEAs. (a) 6.2×10^{10} s^{-1}. (b) 1.2×10^{10} s^{-1}. (c) 6.2×10^{9} s^{-1}. (d) 1.2×10^{9} s^{-1}. (e) 6.2×10^{8} s^{-1}.

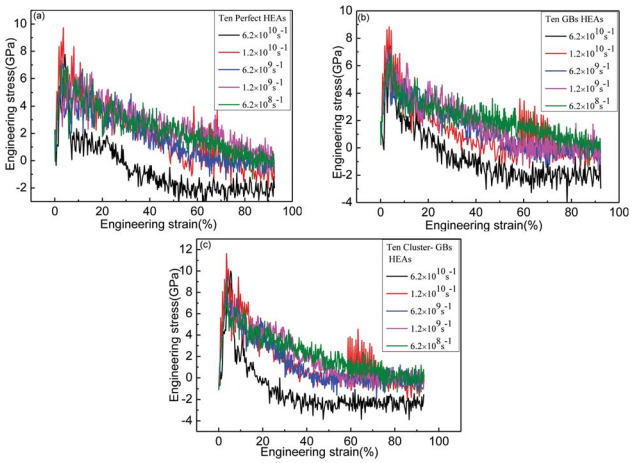

Fig. 7 Tensile engineering stress–strain curves of deformation process oriented in <111> axis under tensile loading at different strain rate. (a) Perfect HEAs. (b) GBs HEAs. (c) Cluster-GBs HEAs.

Deformation behaviour analysis for tensile loading

Fig. 6 presents the tensile engineering stress–strain curves of the atomic structure at different strain rates of the deformation process of perfect HEAs, GBs HEAs and cluster-GBs HEAs oriented in the <111> axis under tensile loading. Perfect HEAs, GBs HEAs and cluster-GBs $Al_{0.1}CoCrFeNi$ HEAs, under the tensile loading perpendicular to the GBs, all displayed linear elastic deformation at low strains, and non-linear elastic deformation at high strains ($\varepsilon > 5\%$). Five curves of stress–strain (Fig. 6(a–e)) show similar stress–strain behaviour, which can be separated into three stages. The first stage is a linear elastic process. As the deformation continues, the stress rises to the peak and then drops down sharply. The third stage is progressive plastic deformation at low stress until the final structure breaks. The stress of cluster-GBs HEAs decreases more than that of other two models in the plastic deformation, that is to say, the decreased magnitude of the stress is the largest. The yield strength and Young's modulus of perfect HEAs, GBs HEAs and cluster-GBs are compared in Table 1. At the same strain rate, cluster-GBs HEAs have a larger yield strength and Young's modulus than that of GBs and perfect HEAs. For perfect HEAs, the dislocations may move quickly without any interference, which cause lower strength in perfect HEAs. For GBs HEAs, GBs may impede dislocation movement, so that the strength is higher than that of perfect HEAs. In cluster-GBs HEAs, high cluster density and GBs impede the dislocation motion, which greatly increases the strength and Young's modulus of cluster-GBs. With increasing strain rate, the yield strength of the three models increases, which also indicates that high strain results in high yield strength.[28–30]

Fig. 7 shows the tensile engineering stress–strain curves at different strain rates for the three models. The higher the strain rate is, the greater the stress reduction rate after yield strength. For the strain rate of 6.2×10^{10} s^{-1}, the decreased magnitude of stress is the largest.

In the FCC crystal structure, there are only four types of dislocation that can occur at GBs according to the Thompson tetrahedron.[31,32] In $Al_{0.1}CrCoFeNi$ $\Sigma3(111)[1\bar{1}0]$ HEAs, the slip plane is also the {111} plane and two different grains are separated by the GBs, which is shown in Fig. 8. For the upper grain, the slip plane is (111), *i.e.*, the ABC plane in the Thompson tetrahedron. ACD, BCD and ABD planes are the other three slip planes. When there is a dislocation at the GBs, it

Table 1 Young's modulus and yield strength of perfect HEAs, GBs HEAs and cluster-GBs HEAs under tensile loading

		6.2×10^{10} s^{-1}	1.2×10^{10} s^{-1}	6.2×10^{9} s^{-1}	1.2×10^{9} s^{-1}	6.2×10^{8} s^{-1}
Young's modulus (GPa)	Perfect	180	208	171	199	213
	GBs	165	233	161	221	198
	Cluster-GBs	212	256	231	266	253
Yield strength (GPa)	Perfect	7.77	7.37	7.0	6.48	6.67
	GBs	7.43	8.56	7.28	6.85	6.88
	Cluster-GBs	10	11	9.49	7.94	9.1

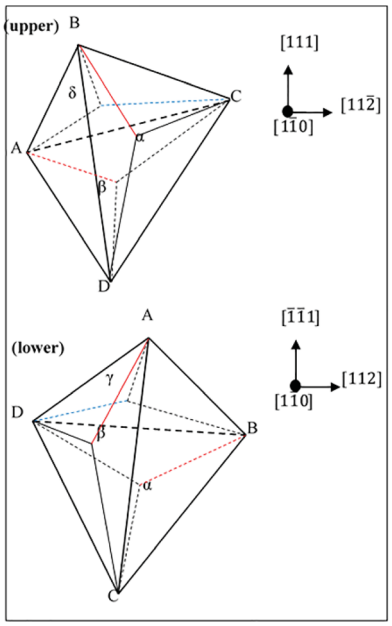

Fig. 8 Thompson tetrahedron for the $Al_{0.1}CoCrFeNi$ Σ3(111)[1$\bar{1}$0] GBs. Two grains in the Thomson tetrahedron are located on the upper and lower sides of GBs. Red color means FCC atoms of dislocation and surface.

is quite possible that the dislocation may slip on one of these three planes. When the dislocation moves to the GBs, the dislocation line would be parallel to the three sides of the ABC slip plane, which is shown as AB, BC or AC. After that, the dislocation can become one of following four types: (1) a 60° perfect dislocation, (2) a 30° Shockley partial dislocation, (3) a 90° Shockley partial dislocation, and (4) a screw perfect dislocation. For the lower grain, the slip plane is ABD and the three slip planes are similar to that of the upper grain, which has been labelled clearly in the lower grain in Fig. 8.

The Thompson tetrahedrons of tensile behaviour for perfect HEAs, GBs HEAs and cluster-GBs oriented in the <111> axis

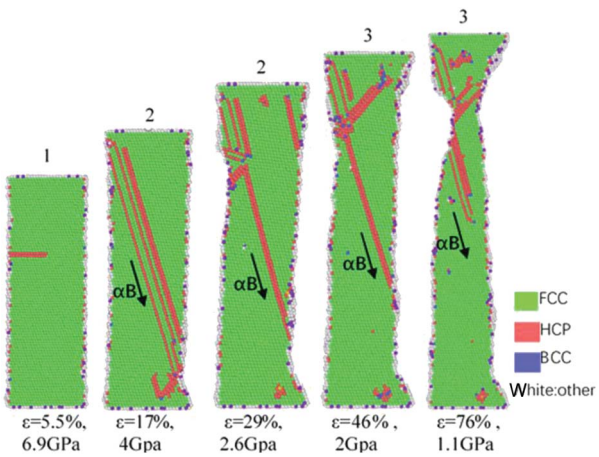

Fig. 9 Tensile behaviour for perfect HEAs with Thompson tetrahedron.

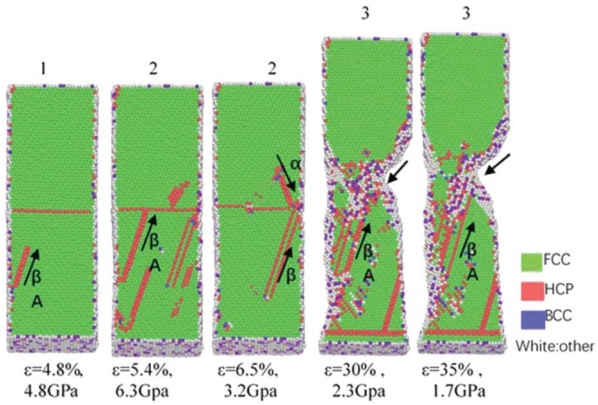

Fig. 10 Tensile behaviour for GBs HEAs with Thompson tetrahedron.

under tensile loading at a strain rate of 6.2×10^8 s^{-1} (Fig. 6(e)) are shown in Fig. 9–11, respectively. The black arrow indicates the direction of dislocation motion at that moment and the specific direction is calibrated on one side. 1, 2 and 3 represent the three stages.

When a tensile loading of perfect HEAs is applied in Fig. 6(e), Fig. 9 indicates that a burgers vector αB, as the leading Shockley partial dislocations, appears in the grain and leads to fracture.

As shown in Fig. 10, there is a leading Shockley partial dislocation with Burgers vector βA appearing in the lower grain at the strain of 4.8%. With increasing strain, the Shockley partial dislocations begin to grow and propagate toward the GBs. When they meet the GBs, some of them disappear (ε = 5.4% in Fig. 10) and some of them merge or meet another Shockley partial dislocation (Burgers vector is αB) coming from the upper grain (ε = 6.5% in Fig. 10). The cross connection for the two Shockley partial dislocations coming from the two opposite grains forms an obvious defect area, which leads to the formation of critical crack sources (ε = 30% and 35% in Fig. 10), destroying the structural integrity of the GBs. The crack further grows and migrates until HEAs are fractured.

In comparison, the HEAs with GBs were quenched in order to form a lot of clusters. For the cluster-GBs HEAs, the deformation behaviour is shown in Fig. 11. It is notable that at this

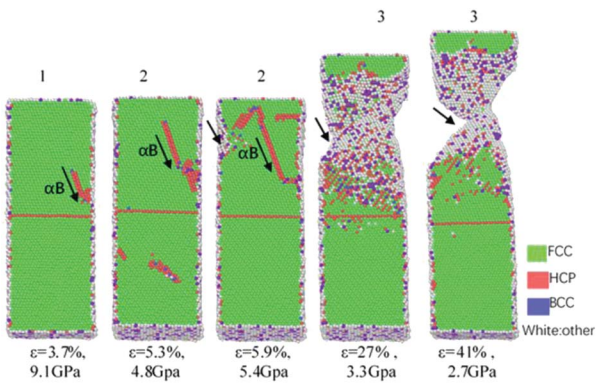

Fig. 11 Tensile behaviour for cluster-GBs with Thompson tetrahedron.

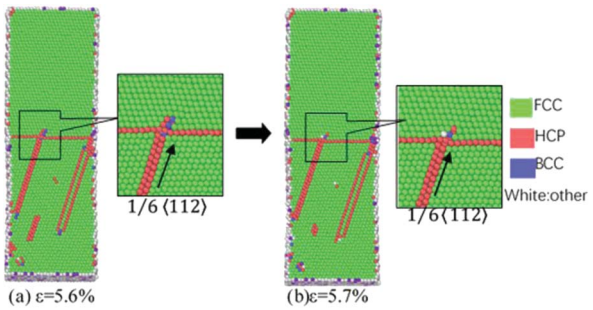

Fig. 12 Nucleation and typical slip of the leading 1/6 <112> Shockley partial dislocations along GB surfaces.

time, the burgers vector αB, as the leading Shockley partial dislocation, appears in the upper grain and moves toward the GBs. For the cluster-GB HEAs, several leading Shockley partial dislocations, which also have different orientations, join together at the intersection point on the left-upper angle (ε = 5.9% in Fig. 11). The intersection point becomes a crack source soon (ε = 27% in Fig. 11). The deformation mechanism is similar to that of the above GB HEAs.

During the deformation process, the detailed mechanism for the deformation and migration of the leading partial dislocations is shown in Fig. 12. It can be seen from Fig. 12 that initially the Shockley partial dislocations of 1/6 <112> nucleate on the {112} plane and then move forward to the GBs with increasing deformation. When these partial dislocations slip and are trapped by the GBs, they try to move along their orientation under tensile loading. However, the atoms on the GBs attempt to block the partial dislocation movement because they have different orientations. Following this, the GB surface begins to deform and form a jog. Finally, the GB surface moves and changes as deformation increases. It also shows that the nucleation and typical slip of the leading Shockley partial dislocations move along the GB surface. It migrates along 1/6 <112> on the {111} plane, which leads to the space variation of partial dislocations. Each nucleation, slip and migration of 1/6 <112> may change one layer for partial dislocation. Therefore, GBs may migrate along the deforming axis.

Deformation behaviour analysis for compressive loading

Fig. 13 presents the compressive engineering stress–strain curves at different strain rates of the deformation process of perfect HEAs, GBs HEAs and cluster-GBs HEAs in the <111> axis. From the curves of Fig. 13(a–e), it can be seen that under the compressive loading, the deformation process of the HEAs is roughly divided into two stages: elastic deformation and uneven plastic deformation (1 and 2 represent two stages). It can be clearly observed that the three structures all show a typical linear elastic mechanism in the process from compressive loading to peak stress. After this stage, the stress–strain curve shows a sudden downward trend and progressive plastic deformation under low stress with continuous loading. At this time, the stress value fluctuates up and down, which belongs to the stage of uneven plastic deformation. Comparison

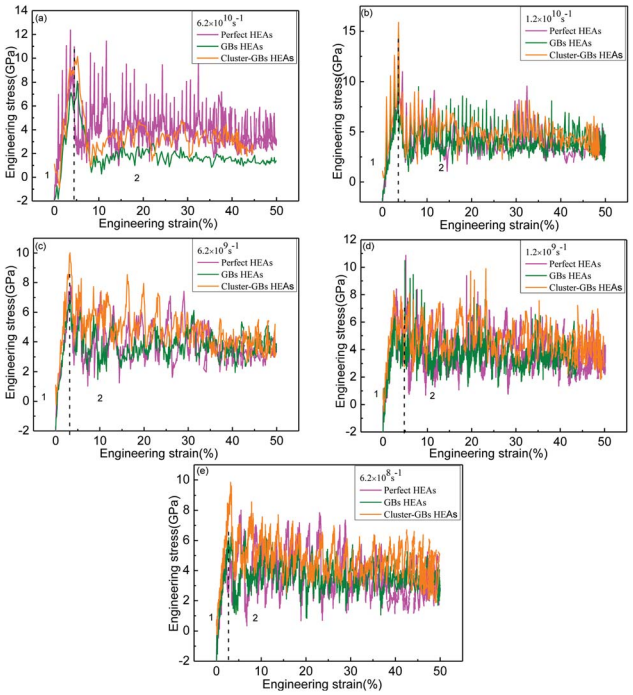

Fig. 13 Compressive engineering stress–strain curves of deformation process oriented in <111> axis under compressive loading at different strain rates for perfect HEAs, GBs HEAs and cluster-GBs HEAs. (a) 6.2 × 10^{10} s^{-1}. (b) 1.2 × 10^{10} s^{-1}. (c) 6.2 × 10^{9} s^{-1}. (d) 1.2 × 10^{9} s^{-1}. (e) 6.2 × 10^{8} s^{-1}.

among the three compressive engineering stress–strain curves shown in Fig. 13(a) reveals that the perfect HEAs exhibit a larger fluctuation amplitude than the GBs and cluster-GBs HEAs at a strain rate of 6.2 × 10^{10} s^{-1}. The reason may be that there is no defect in perfect HEAs and the critical stress is higher. It is difficult to start a slip system. Once the first slip system starts, the slip speed is fast. When this slip speed slows down, it is possible that twins appear and other slip systems start to slip,

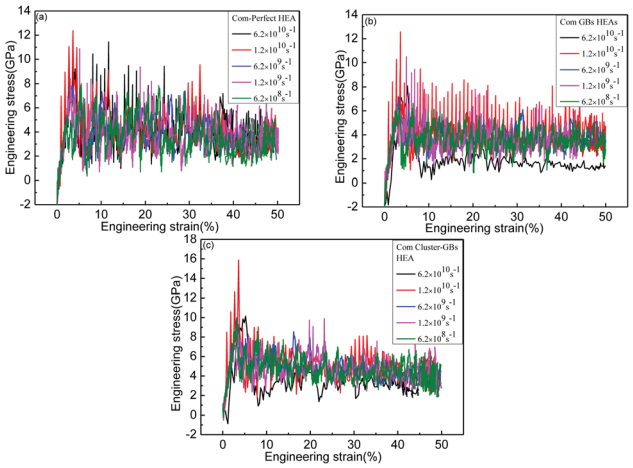

Fig. 14 Compressive engineering stress–strain curves of deformation process oriented in <111> axis under compressive loading at different strain rates. (a) Perfect HEAs. (b) GBs HEAs. (c) Cluster-GBs HEAs.

Table 2 Young's modulus and yield strength of perfect HEAs, GBs HEAs and cluster-GBs HEAs under compressive loading

		6.2×10^{10} s^{-1}	1.2×10^{10} s^{-1}	6.2×10^{9} s^{-1}	1.2×10^{9} s^{-1}	6.2×10^{8} s^{-1}
Young's modulus (GPa)	Perfect	248	252	250	260	266
	GBs	251	249	246	244	253
	Cluster-GBs	229	285	299	292	276
Yield strength (GPa)	Perfect	8.67	8.12	7.79	7.86	5.36
	GBs	8.1	6.99	7.11	6.16	6.18
	Cluster-GBs	10.13	11.86	10.01	8.28	9.59

and the whole system continues to slip substantially. It is shown in Fig. 13 that the yield strength and Young's modulus of perfect HEAs are higher than that of GBs HEAs. The yield strength and Young's modulus of cluster-GBs HEAs are both still the largest, which also proves that cluster and GBs would increase the yield strength of HEAs.[33–35]

The compressive engineering stress–strain curves at different strain rates for three structures are presented in Fig. 14. The variation trend is very similar to that of tensile strength. The higher the strain rate is, the greater the stress reduction rate. No matter which model, the decreased magnitude of the stress is the largest when the strain rate is 6.2×10^{10} s^{-1}. The yield strength and Young's modulus of perfect HEAs, GBs HEAs and cluster-GBs are listed in Table 2.

Under compressive loading, the Thompson tetrahedrons of tensile behaviour for perfect HEAs, GBs HEAs and cluster-GBs oriented in <111> axis at a strain rate of 6.2×10^{8} s^{-1} (Fig. 13(e)) are also dominated by Shockley partial dislocation, which is shown in Fig. 15–17, respectively. In Fig. 15, βA Shockley partial dislocations of 1/6 <112> nucleate and control the deformation of HEAs. In Fig. 16, in the initial stage, βA Shockley partial dislocations nucleate first in the lower grain and grow upward to GBs at the strain of 3.3%. βA Shockley partial dislocations continue to growth and want to reach GBs at the strain of 31.3%. After that, αB Shockley partial dislocations occur to slip in the upper grain ($\varepsilon = 44.4\%$ in Fig. 16). With increasing compressive loading, the Shockley partial dislocations merge with each other near the GBs and cause it to distort. At the same time, point defects, such as vacancies or interstitials, are observed in the compressive deformation, which is shown in Fig. 16 (where the arrow points when ε is 31.3%).

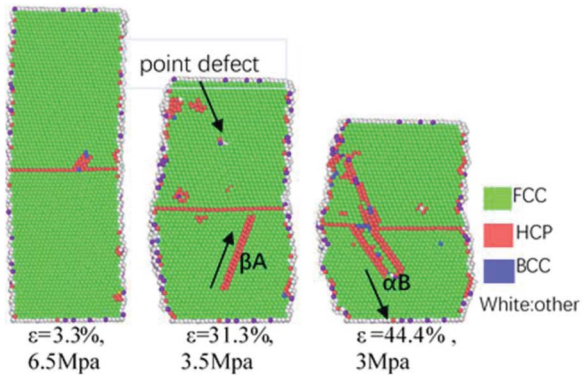

Fig. 16 Compressive behaviour for GBs HEAs with Thompson tetrahedron. Different color means different crystal structure.

The main dislocations are βA and αB Shockley partial dislocations in the deformation of perfect HEAs and GBs HEAs. However, in the compressive behaviour of cluster-GBs HEAs in Fig. 17, it is clearly observed that Aβ and αB Shockley partial dislocations move downward to the cluster-GBs and are blocked by cluster-GBs ($\varepsilon = 23\%$ in Fig. 17). Aβ and αB Shockley partial dislocations form 60°, which could arrest crack propagation. Furthermore, due to the distortion of cluster-GBs HEAs,

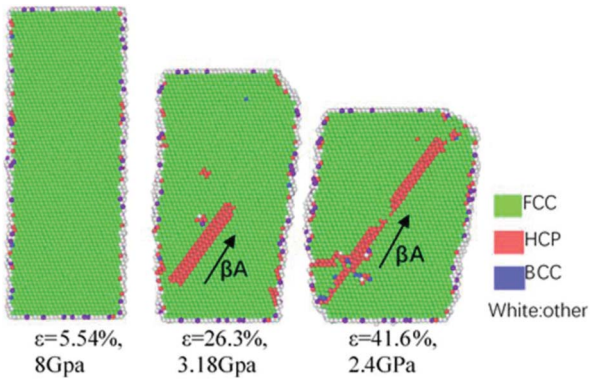

Fig. 15 Compressive behaviour for perfect HEAs with Thompson tetrahedron.

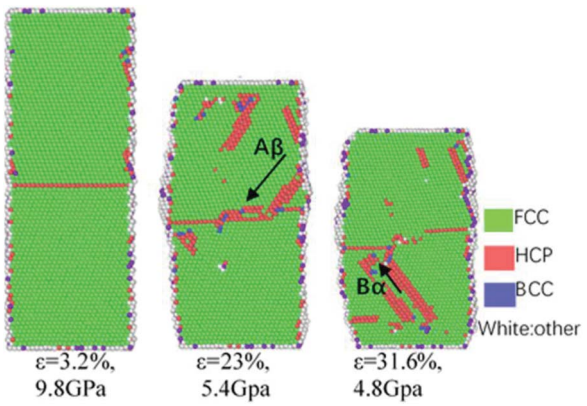

Fig. 17 Compressive behaviour for cluster-GBs HEAs with Thompson tetrahedron.

deformation for HEAs becomes difficult. This is the reason why cluster-GBs HEAs have the largest yield strength and Young's modulus.

Conclusions

In the present study, the deformation processes of the three forms of $Al_{0.1}CoCrFeNi$ $\Sigma3(111)[1\bar{1}0]$ HEAs under tensile and compressive loading conditions were discussed. The quasi-static stretch, as an applied tensile and compressive loading, was imposed in the three models including perfect HEAs, GBs HEAs and cluster-GBs HEAs, which were oriented in the <111> axis with different strain rates, including 6.2×10^{10} s^{-1}, 1.2×10^{10} s^{-1}, 6.2×10^{9} s^{-1}, 1.2×10^{9} s^{-1} and 6.2×10^{8} s^{-1}, using MD simulations methods. The deformation mechanism for the HEAs under the tensile and compressive loading was studied. The main results show that under tensile loading, the three models all display three stages. The first stage is a linear elastic process. As the deformation continues, the stress rises to the peak and then drops down sharply. The third stage is progressive plastic deformation at low stress until the final structure breaks. The cluster-GBs HEAs display the largest decreased magnitude in the plastic deformation. At the same strain rate, cluster-GBs HEAs have the largest yield strength and Young's modulus. The higher the strain rate is, the greater the stress reduction rate. Under compressive loading, two behaviour stages of deformation are analyzed. Cluster-GBs HEAs also have the largest yield strength.

Under tensile or compressive loadings, the Shockley partial dislocations of 1/6 <112> were observed as the leading dislocation to slip during the deformation. However, there are different partial dislocations on the upper and lower grains. Their cross connections always become a crack source. The GBs always block the movement of those partial dislocations, while the partial dislocations distort the GBs. This deformation mechanism may be the main reason to lead to the extreme strength of HEAs.

Conflicts of interest

There are no conflicts to declare.

Acknowledgements

This work was financially supported by the Natural Science Foundation of China (No. 51971166) and Key Laboratory of Shaanxi Provincial Education Department (No. 20JS055).

References

1 M. H. Tsai and J. W. Yeh, *Mater. Res. Lett.*, 2014, **2**(3), 107–123.
2 J. W. Yeh, S. K. Chen, S. J. Lin, J. Y. Gan, T. S. Chin, T. T. Shun, C. H. Tsau and S. Y. Chang, *Adv. Eng. Mater.*, 2004, **6**, 299–303.
3 Y. Zhang, T. Zuo, Y. Cheng and P. K. Liaw, *Sci. Rep.*, 2013, **3**, 1455.
4 B. Gludovatz, A. Hohenwarter, D. Catoor, E. H. Chang, E. P. George and R. O. Ritchie, *Science*, 2014, **345**, 1153–1158.
5 M. A. Hemphill, T. Yuan, G. Y. Wang, J. W. Yeh, C. W. Tsai, A. Chuang and P. K. Liaw, *Acta Mater.*, 2012, **60**, 5723–5734.
6 D. Li, H. L. Hou, Z. Xi, C. H. Chen and M. Li, *Review on Ballistic Impact Resistance of Ship Armor Protection Structure, Shipbuilding of China*, 2018, 59, PP. 237–248.
7 C. Zhang, F. Zhang, H. Y. Diao, M. C. Gao, Z. Tang, J. D. Poplawsky and P. K. Liaw, *Mater. Des.*, 2016, **109**, 425–433.
8 L. J. Santodonato, Y. Zhang, M. Feygenson, C. M. Parish, M. C. Gao, R. J. K. Weber, J. C. Neuefeind, Z. Tang and P. K. Liaw, *Nat. Commun.*, 2015, **6**, 5964.
9 Y. Zhang, T. T. Zuo, Z. Tang, M. C. Gao, K. A. Dahmen, P. K. Liaw and Z. P. Lu, *Prog. Mater. Sci.*, 2014, **61**, 1–93.
10 A. Sharma, P. Singh, D. D. Johnson, P. K. Liaw and G. Balasubramanian, *Sci. Rep.*, 2016, **6**, 31028.
11 F. Otto, A. Dlouhy, C. Somsen, H. Bei, G. Eggler and E. P. George, *Acta Mater.*, 2013, **61**, 5743–5755.
12 M. D. Sangid, T. Ezaz, H. Sehitoglu and I. M. Robertson, *Acta Mater.*, 2011, **59**(1), 283–296.
13 Q. Q. Ding, Y. Zhang, X. Chen, X. Q. Fu, Q. Yu, *et al.*, *Nature*, 2019, **574**, 223.
14 X. Lu, P. Brault, A. L. Thomann and J. M. Bauchire, *Appl. Surf. Sci.*, 2013, 26276.
15 J. C. Huang, S. H. Chang and H. P. Chen, *Adv. Mater. Res.*, 2012, **579**, 398–406.
16 Y. Li, M. Lv and H. Y. Liang, *J. Comput. Theor. Nanosci.*, 2015, **12**, 4649–4653.
17 Y. C. Yang, C. X. Liu, C. Y. Lin and Z. H. Xia, *Scr. Mater.*, 2020, **178**, 181–186.
18 H. Y. Yasuda, H. Miyamoto, K. Cho and T. Nagase, *Mater. Lett.*, 2017, **199**, 120–123.
19 D. G. Brandon, *Acta Metall.*, 1966, **14**, 1479–1484.
20 Q. Yin, Z. Q. Wang, R. Mishra and Z. H. Xia, *AIP Adv.*, 2017, **7**(1), 015040.
21 P. R. M. van Beers, V. G. Kouznetsova, M. G. D. Geers, M. A. Tschopp and D. L. McDowell, *Acta Mater.*, 2015, **82**, 513–529.
22 B. Schönfelder, D. Wolf, S. R. Phillpot and M. Furtkamp, *Interface Sci.*, 1997, **5**, 245–262.
23 J. Wang, N. Li and A. Misra, *Magazine*, 2013, **93**, 315–327.
24 M. S. Daw and M. I. Baskes, *Phys. Rev. Lett.*, 1983, **50**(17), 1285–1288.
25 M. S. Daw and M. I. Baskes, *Phys. Rev. B: Condens. Matter Mater. Phys.*, 1984, **29**(12), 6443–6453.
26 S. Plimpton, *J. Comput. Phys.*, 1995, **117**, 1–19.
27 A. Stukowski, *Modell. Simul. Mater. Sci. Eng.*, 2010, **18**, 015012.
28 G. Sainath and B. K. Choudhary, *Phys. Lett. A*, 2015, **379**, 1902–1905.
29 P. T. Li, Y. Q. Yang, Z. H. Xia, X. Luo, N. Jin, Y. Gao and G. Liu, *RSC Adv.*, 2017, **7**, 48315–48323.
30 G. J. Shi, J. G. Wang, Z. Y. Hou, *et al.*, *Mod. Phys. Lett. B*, 2017, **31**(27), 1750247.
31 G. Sainath and B. K. Choudhary, *Philos. Mag.*, 2016, **96**(32–34), 3502–3523.

32 A. Stukowski and K. Albe, *Modell. Simul. Mater. Sci. Eng.*, 2010, **18**, 025016.
33 M. Feuerbacher, M. Heidelmann and C. Thomas, *Philos. Mag.*, 2015, **95**, 1221–1232.
34 Y. T. Zhu, X. L. Wub, X. Z. Liao, J. Narayan a, L. J. Kecskés and S. N. Mathaudhu, *Acta Mater.*, 2011, **59**, 812–821.
35 A. J. Cao, Y. G. Wei and S. X. Mao, *Appl. Phys. Lett.*, 2007, **90**, 151909.